MNRAS **000**, 000–000 (0000) Preprint 20 December 2021 Compiled using MNRAS LATEX style file v3.0

On effects of surface bipolar magnetic regions on the convection zone dynamo

V.V. Pipin*
Institute of Solar-Terrestrial Physics, Russian Academy of Sciences, Irkutsk, 664033, Russia

20 December 2021

ABSTRACT

We investigate the effect of the surface tilted bipolar magnetic regions (BMR) on the large-scale dynamo distributed in the bulk of the convection zone. The study employs the nonlinear 3D mean-field dynamo model. The emergence of the BMR on the surface is modeled by means of the nonaxisymmetric magnetic buoyancy effect which acts on the large-scale toroidal magnetic field in the upper half of the convection zone. The nonaxisymmetric magnetic field which results from this mechanism is shallow. At the surface the effect of the BMR on the magnetic field generation is dominant. However, because of the shallow BMR distribution, its effect on the global dynamo is moderate. The most dynamo effect of the surface BMR is due to their evolution and the convective zone α effect. The fluctuations of the BMR's tilt affect the equatorial symmetry of the dynamo-generated magnetic field. In agreement with the solar observations, the emerging BMRs result in the negative magnetic helicity density of the large-scale nonaxisymmetric magnetic fields in the northern hemisphere of the star.

Key words: Sun: magnetic fields; Sun: oscillations; sunspots

1 INTRODUCTION

The basic properties of the solar dynamo, which operates deep in the solar convection zone, are encoded in the properties of the surface sunspot activity and their magnetic fields. In about every 10-11 years, the sunspots, mostly in form of the bipolar magnetic regions (BMR), appear on the solar surface. The sign of the leading BMRs' polarity, in general, satisfies the Hale polarity law. The BMRs tend to be tilted relative to the equator (Hale et al. (1919)). Parker (1955a); Parker (1955b) formulated the basic idea of the solar hydromagnetic dynamo. It was suggested that the sunspots are formed from the large-scale toroidal magnetic field, which resides deep in the convection zone. In the large-scale dynamo the toroidal magnetic field is transformed cyclically to the poloidal magnetic field through cyclonic convection. It is regenerated back with the opposite sign through the differential rotation. The whole dynamo process can be represented as the dynamo waves propagating through the convection zone. This idea grew to the mean-field MHD and dynamo theory (Moffatt (1978); Krause & Rädler (1980)). The mean-field theory framework employs the idea of the scale separation between the mean and turbulent parts of the magnetic field and flows. It assumes that the mean large-scale field can be extracted from the background turbulent astrophysical plasma utilizing an appropriate averaging procedure (see, the above-cited textbooks). In the solar-type dynamos, the axisymmetric magnetic field dominates. On the Sun the large-scale nonaxisymmetric dynamo is well below the dynamo instability threshold because of differential rotation (Raedler (1986)). Yet, most of the energy of the surface magnetic field is concentrated on small scales (Vidotto et al. 2018) . The origin of the surface nonaxisymmetric magnetic fields seems to be connected with emergence and decay of solar active regions (Mackay & Yeates 2012; Hathaway 2015).

The effect of the surface magnetic activity on the large-scale dynamo is poorly understood. One way to account for it is through the boundary conditions. Under the insulator boundary condition, the external magnetic field is potential, and the toroidal magnetic field is zero at the surface. Observations show that more realistic boundary conditions should be used to allow penetration of the toroidal magnetic field to the surface (Moss & Brandenburg (1992); Bonanno (2016)). Note, that the penetration of the toroidal magnetic field to the surface allows the efficient poloidal magnetic field generation in the near-surface layer.

Another way to account for the surface magnetic activity on the dynamo is employed in the Babcock-Leighton scenario (Babcock 1961 and Leighton 1964). The phenomenological picture behind it was established and summarized in the number of papers and reviews (see, e.g., Giovanelli 1985; Wang et al. 1989; Petrie et al. 2014). This scenario is employed in the flux

* email: pip@iszf.irk.ru

transport dynamo models (Mackay & Yeates 2012; Ugarte-Urra et al. 2015; Cameron & Schüssler 2017 and references therein). In this scenario, the tilted BMRs emerging and evolving at the surface result in the dynamo generation of the poloidal magnetic field of the Sun. In the convection zone dynamo scenario, the regeneration of the poloidal magnetic field goes everywhere in the depth of the convection zone.

Results of the flux transport dynamo models (see, Karak et al. 2014; Passos et al. 2014; Hazra & Nandy 2019) show the necessity of the mean-field effects to account for the possible complicated properties of the global flows and properties of the long-term variations of the solar activity. Yet, the simple framework of the Babcock-Leighton scenario faces problems to reproduce the results of the global convection dynamo simulation (see, Schrinner (2011); Schrinner et al. (2011); Warnecke et al. (2021)). This is due to a poor representation of the mean electromotive force of turbulent flows and magnetic fields. In this paper, we consider the mean-field dynamo model of Pipin & Kosovichev (2019). To account for the surface magnetic activity in form of the tilted bipolar magnetic regions the model prescribes the nonaxisymmetric magnetic buoyancy and α effects acting on the large-scale toroidal magnetic field. This extension of the mean-field model was introduced earlier by Pipin (2021) and Obridko et al. (2021) to explain the surface magnetic field helicity evolution and the phase shifts between the zonal harmonics of the poloidal magnetic field of the Sun. Here, we extend our study further by looking at the dynamo effects of the surface BMR.

2 DYNAMO MODEL

We model the magnetic field evolution using the mean-field induction equation Krause & Rädler (1980):

$$\partial_t \langle \mathbf{B} \rangle = \nabla \times \left(\mathcal{E} + \langle \mathbf{U} \rangle \times \langle \mathbf{B} \rangle \right) , \tag{1}$$

where $\mathcal{E} = \langle \mathbf{u} \times \mathbf{b} \rangle$ is the mean electromotive force; $\mathbf{u}$ and $\mathbf{b}$ are the turbulent fluctuating velocity and magnetic field, respectively; and $\langle \mathbf{U} \rangle$ and $\langle \mathbf{B} \rangle$ are the mean velocity and magnetic field. Like Moss et al. (1991), we represent the vector $\langle \mathbf{B} \rangle$ by sum of the axisymmetric and nonaxisymmetric parts, which are decomposed into sum of the poloidal and toroidal components, as follows:

$$\langle \mathbf{B} \rangle = \overline{\mathbf{B}} + \tilde{\mathbf{B}} , \tag{2}$$

$$\overline{\mathbf{B}} = \hat{\phi} B + \nabla \times \left(A \hat{\phi} \right) , \tag{3}$$

$$\tilde{\mathbf{B}} = \nabla \times (\mathbf{r} T) + \nabla \times \nabla \times (\mathbf{r} S) , \tag{4}$$

where $\overline{\mathbf{B}}$ and $\tilde{\mathbf{B}}$ are the axisymmetric and nonaxisymmetric components, A, B, T and S are the scalar functions representing the field components, $\hat{\phi}$ is the azimuthal unit vector, $\mathbf{r}$ is the radius vector, r is the radial distance, and θ is the polar angle. The gauge transformation for potentials T and S involves a sum with the arbitrary r-dependent function (Krause & Rädler 1980). We use spherical harmonic decomposition for superpotentials T and S. For them, by definition, the zero ℓ modes are excluded. In this case, the representation of the Eq(4) is gauge invariant (also, see, Berger & Hornig 2018).

The turbulent effects on the mean magnetic field evolution are described by the mean electromotive force. We use the same formulation as Obridko et al. (2021):

$$\mathcal{E}_i = \mathcal{E}_i^{(A)} + \mathcal{E}_i^{(P)} , \tag{5}$$

where the mean electromotive force is divided into the "standard" $\mathcal{E}_i^{(A)}$, and phenomenological parts, $\mathcal{E}_i^{(P)}$. The $\mathcal{E}_i^{(A)}$ was obtained analytically (see, (Kitchatinov et al. 1994; Pipin 2008)). It contains contributions of the turbulent generation by α-effect (the tensor, α_{ij}), the turbulent pumping is accounted by means tensor γ_{ij} and η_{ijk} is the eddy magnetic diffusivity tensor:

$$\mathcal{E}_i^{(A)} = (\alpha_{ij} + \gamma_{ij}) \langle B \rangle_j - \eta_{ijk} \nabla_j \langle B \rangle_k . \tag{6}$$

Here, the mean-field analytical expressions of the α_{ij} and γ_{ij} account for effects of the global rotation, magnetic field density stratification. Also, we take into account the anisotropy of the eddy diffusivity due to the effect of the global rotation. The details about analytical calculations of the turbulent coefficients can be found in the above-cited papers. The same model was recently considered by Pipin & Kosovichev (2019) and Pipin & Kosovichev (2020), where the reader can find the further details concerning $\mathcal{E}_i^{(A)}$.

To account for the effects of the surface the bipolar magnetic regions (BMRs) on the dynamo, in the depth of the convection zone, we introduce the phenomenological part of the mean-electromotive force as follows,

$$\mathcal{E}_i^{(P)} = \alpha_\beta \delta_{i\phi} \langle B \rangle_\phi - V_\beta \left(\hat{\boldsymbol{r}} \times \langle \mathbf{B} \rangle \right)_i , \tag{7}$$

where the first term accounts for the α effect of the BMRs and the second term accounts for the magnetic buoyancy effect. Following Parker (1984), we assume that some part of the toroidal magnetic field in the the upper part becomes unstable and it forms magnetic BMRs on the solar surface. The mechanism of this instability can be rather difficult (see, e.g., Gilman

1970, 2018). Also, it is likely, that there are other processes in the solar convection zone that can be responsible for the BMRs formations (see, e.g.,Kleeorin et al. 1989; Kitchatinov & Mazur 2000; Getling 2001; Brandenburg et al. 2013; Stein & Nordlund 2012; Losada et al. 2017; Kleeorin et al. 2020). We employ the magnetic buoyancy effect in a formal way to mimic the BMRs on the solar surface. The other implementations of the BMRs in the dynamo models can be found in the models of the Babcock-Leighton type (see, e.g., Yeates et al. 2008; Brun et al. 2014). Following Pipin (2021), we put

$$V_\beta = -\frac{\alpha_{\rm M} u_c}{\gamma}\left(\beta^2 K(\beta) + \beta_m^2 K(\beta_m)\,\xi_\beta(t,\boldsymbol{r})\right), \quad (8)$$

where $\alpha_{\rm M} = 1.9$ is the mixing-length theory parameter, γ is the adiabatic law constant, u' is the convective RMS velocity function $K(\beta)$ is given in Kitchatinov & Pipin (1993).The first term in the Eq(8) determines the standard mean-field magnetic buoyancy effect, see the above-cited paper. The parameter ξ_β determines the magnetic buoyancy velocity perturbations, the subscript 'm' marks that the amplitude of the effect is taken at the location of the magnetic field maximum. The position of the unstable layer was computed following the consideration of Parker (1979). It is assumed that the large-scale toroidal magnetic field becomes unstable when its strength decreases outward faster than the mean density does. In particular, we compute the parameter

$$I = -r\frac{\partial}{\partial r}\log\frac{|\overline{B}|^\zeta}{\overline{\rho}}, \quad (9)$$

where $\overline{B}$ is the strength of the toroidal magnetic field and $\overline{\rho}$ is the density profile. The unstable part of the toroidal magnetic field satisfies $I > 0$. Note, that the magnetic buoyancy instability can be affected by the stellar turbulence and the global rotation (Gilman 1970; Acheson & Gibbons 1978; Davies & Hughes 2011; Gilman 2018). For the case of $\zeta = 1$ we get the Parker's instability condition. With $\zeta = 1$, the instability condition is rather severe for upper part of the convection zone. In this case we find that BMR production is not sufficient to reproduce the solar observations with our dynamo model. In our simulations we use $\zeta = 1.2$. The dependence of ζ parameter on the physical conditions in the stellar convection zone deserves a separate study and it is out of our scope for this paper.

The nonaxisymmetric perturbations, ξ_β, are randomly initiated in time and longitude within the upper layer of the convection zone. We assume that can be $\xi_\beta > 0$ for the $r > 0.85R$ only if the toroidal magnetic field strength is above 500 G. The ξ_β represent the gaussian process in time with the mean cadence equal to about half month. The choice is rather arbitrary. The model with the shorter time cadence of the ξ_β produces the more BMRs and the larger surface magnetic flux. However, the short cadence may result in BMRs overlap. This depends on the spatial size of the generated BMRs. It is controlled by the formula,

$$\xi_\beta = \psi\exp\left(-m_\beta\left(\sin^2\left(\frac{\phi-\phi_m}{2}\right)+\sin^2\left(\frac{\theta-\theta_{\rm m}}{2}\right)\right)\right), \quad (10)$$

where ψ is a kink-type function in radius and time,

$$\begin{aligned}\psi &= \frac{1}{2}\left(1-{\rm erf}\left(50\left(r-r_m\right)\right)\right){\rm e}^{-\frac{t}{\tau_0}}, t<\delta t \\ &= 0, t>\delta t\,,\end{aligned} \quad (11)$$

where r_m and θ_m are the radius and the latitude of the toroidal magnetic field strength extrema in the upper part of the convection zone; the longitude ϕ_m is random. Similar to our previous paper we restrict δt to one week. The emergence interval of the BMRs is controlled by the parameter τ_0. In our simulations, we put it to 3 days, which corresponds to the observation results (see, Stenflo & Kosovichev 2012; Stenflo 2013). In the paper we put $m_\beta = 50$. The α-effect will be given as follows

$$\alpha_\beta = \xi_\alpha \cos\theta V_\beta, \quad (12)$$

where V_β is determined by Eq(8). The amplitude of the α-effect is determined by the local magnetic buoyancy velocity. The ξ_α parameter introduce the random fluctuation of the BMRs α-effect. Similar to Pipin & Kosovichev (2020) we model the random parameter ξ_α via Ornstein–Uhlenbeck process,

$$\begin{aligned}\dot{\xi}_\alpha &= -\frac{2}{\tau_\xi}\left(\xi_\alpha - \xi_1\right), \\ \dot{\xi}_1 &= -\frac{2}{\tau_\xi}\left(\xi_1 - \xi_2\right), \\ \dot{\xi}_2 &= -\frac{2}{\tau_\xi}\left(\xi_2 - g\sqrt{\frac{2\tau_\xi}{\tau_h}}\right),\end{aligned}$$

where g is a Gaussian random number which is renewed at every time step, τ_h is the time step of the numerical simulations, τ_ξ is the relaxation time of ξ_α and $\xi_{1,2,3}$ are auxiliary parameters that are introduced to smooth variations of ξ_α with its first- and second-order derivatives. Similarly to the above cited papers we choose the parameters of the gaussian process as folows, $\overline{g} = 1$, $\sigma(g) = 1$ and $\tau_\xi = 3$ months. The parameters ξ_α and ξ_β set to vary independently in the northern and southern hemispheres. For the given choice the tilt of the BMRs is about 7° at 15° latitude (Tlatov et al. (2013)). Our model of the tilted BMR

is rather simplistic and it is restricted by the mean-field framework. Kleeorin et al. (2020) suggested a more elaborated and consistent approach, which would be interesting to undertake in a future studies.

With our representation of the mean electromotive force in the form of Eq(5), the full version of the dynamo equations for the axisymmetric magnetic field reads as follows,

$$\begin{aligned}\partial_t A &= \mathcal{E}_\phi^{(A)} + \overline{\alpha_\beta \langle B_\phi \rangle} + \frac{V_\beta}{r}\frac{\partial (rA)}{\partial r} + \overline{V_\beta \tilde{B}_\theta} \\ &+ \frac{U_\theta}{r}\frac{\partial A \sin\theta}{\partial \mu} - \frac{U_r}{r}\frac{\partial Ar}{\partial r} \end{aligned} \tag{13}$$

$$\begin{aligned}\partial_t B &= \frac{\sin\theta}{r}\frac{\partial (r\sin\theta A, \Omega)}{\partial (r,\mu)} - \frac{1}{r}\frac{\partial}{\partial r} r^2 \left(V_\beta B + \overline{V_\beta \tilde{B}_\phi} \right) \\ &+ \frac{1}{r}\frac{\partial r \mathcal{E}_\theta^{(A)}}{\partial r} + \frac{\sqrt{(1-\mu^2)}}{r}\frac{\partial \mathcal{E}_r^{(A)}}{\partial \mu} \\ &+ \frac{\sin\theta}{r}\frac{\partial U_\theta B}{\partial \mu} - \frac{1}{r}\frac{\partial r U_r B}{\partial r}, \end{aligned} \tag{14}$$

where, the contribution of $\mathcal{E}^{(A)}$ stands for the standard part of the mean-electromotive force, its details are omitted. The nonaxisymmetric part of the dynamo equations was given in our previous paper (see, Obridko et al. 2021). The primary goal of the paper is to study the effects of the surface bipolar magnetic region evolution on the large-scale dynamo. Generally, we can identify the contributions of two types. One is generation effects which are represented by the $\overline{\alpha_\beta \langle B \rangle_\phi}$ term and the other contributions, like $\overline{V_\beta \tilde{B}_\theta}$, and $\overline{V_\beta \tilde{B}_\phi}$ results to the dynamo quenching due to the magnetic flux loss by means of the magnetic buoyancy. Also, both of these processes are mediated by the surface magnetic field evolution. For example, the nonaxisymmetric magnetic field evolving on the solar surface can result in the large-scale poloidal magnetic field generation via the standard mean-field α-effect. The α effect generation in the Eq.(13) described by the sum,

$$\overline{\alpha \langle B \rangle_\phi} = \overline{\alpha} B + \overline{\tilde{\alpha} \tilde{B}_\phi} + \overline{\alpha_\beta \langle B \rangle_\phi}, \tag{15}$$

where the first term is the standard part of the mean-field dynamo equations. The others are due to the nonaxisymmetric magnetic field. In the first term, the coefficient $\overline{\alpha}$ reads

$$\overline{\alpha} = C_\alpha \psi_\alpha(\beta) \alpha_{\phi\phi}^{(H)} + \alpha_{\phi\phi}^{(M)} \psi_\alpha(\beta) \frac{\overline{\chi} \tau_c}{4\pi \overline{\rho} \ell_c^2}, \tag{16}$$

where contributions of the kinetic α effect tensor $\alpha_{ij}^{(H)}$ and the magnetic helicity effect tensor $\alpha_{ij}^{(M)}$ are given in Pipin (2018). Their radial profiles depend on the mean density stratification, profile of the convective RMS velocity u_c and on the Coriolis number $\Omega^* = 2\Omega_0 \tau_c$, where the Ω_0 is the angular velocity of the star and τ_c is the convective turnover time. The magnetic quenching function $\psi_\alpha(\beta)$ depends on the parameter $\beta = \left|\overline{\mathbf{B}}\right| / \sqrt{4\pi\overline{\rho} \mathrm{u}_\mathrm{c}^2}$. It is given in the above cited paper. For the large $\left|\overline{\mathbf{B}}\right|$, when $\beta \gg 1$, $\psi_\alpha(\beta) \sim \beta^{-3}$. The other parts in the Eq.(16) represent the magnetic helicity density $\overline{\chi} = \overline{\mathbf{a} \cdot \mathbf{b}}$ ($\mathbf{a}$ and $\mathbf{b}$ are the turbulent parts of the magnetic vector potential and magnetic field vector), the convective mixing length ℓ_c, the mean density, $\overline{\rho}$, and C_α is the control dynamo parameter of the kinetic α effect. The nonaxisymmetric $\tilde{\alpha}$ in the Eq(15) results from nonlinear contributions of the large-scale magnetic field in the Eq(16). The $\tilde{\alpha}$ is zero for the case of the linear dynamo.

We model the magnetic helicity evolution using the global conservation law for the total magnetic helicity, $\langle \chi \rangle = \langle \mathbf{a} \cdot \mathbf{b} \rangle$, (see, Hubbard & Brandenburg (2012); Pipin et al. (2013); Brandenburg (2018)):

$$\left(\frac{\partial}{\partial t} + \langle \mathbf{U} \rangle \cdot \boldsymbol{\nabla} \right) \langle \chi \rangle^{(tot)} = -\frac{\langle \chi \rangle}{R_m \tau_c} - 2\eta \langle \mathbf{B} \rangle \cdot \langle \mathbf{J} \rangle - \nabla \cdot \mathcal{F}^\chi, \tag{17}$$

where $\langle \chi \rangle^{(tot)} = \langle \chi \rangle + \langle \mathbf{A} \rangle \cdot \langle \mathbf{B} \rangle$ is the total magnetic helicity density of the mean and turbulent fields. Note, that in derivations of the Eq.(17), in following Kleeorin & Rogachevskii (1999), we have $2\eta \langle \mathbf{b} \cdot \mathbf{j} \rangle = \frac{\langle \chi \rangle}{R_m \tau_c}$. Also, $\mathcal{F}^\chi = -\eta_\chi \nabla \langle \chi \rangle^{(tot)}$ is the diffusive flux of the total magnetic helicity, and R_m is the magnetic Reynolds number. The coefficient of the turbulent helicity diffusivity, η_χ, is chosen ten times smaller than the isotropic part of the magnetic diffusivity Mitra et al. (2010): $\eta_\chi = \frac{1}{10}\eta_T$. Note, that papers of Kleeorin & Ruzmaikin (1982); Kleeorin & Rogachevskii (1999) suggested a different ansatz. The dynamo model that involves the magnetic helicity conservation in form of the Eq(17) shows the magnetic helicity patterns which propagate with the dynamo wave through the bulk of the convection zone (Pipin et al. 2013).

The mean magnetic helicity density is formally decomposed into the axisymmetric and nonaxisymmetric parts: $\langle \chi \rangle^{(tot)} = \overline{\chi}^{(tot)} + \tilde{\chi}^{(tot)}$. The same is done for the magnetic helicity density of the turbulent field: $\langle \chi \rangle = \overline{\chi} + \tilde{\chi}$, here $\overline{\chi} = \overline{\mathbf{a} \cdot \mathbf{b}}$ and $\tilde{\chi} = \langle \tilde{\mathbf{a}} \cdot \tilde{\mathbf{b}} \rangle$. Thus, we have,

$$\overline{\chi}^{(tot)} = \overline{\chi} + \overline{\mathbf{A}} \cdot \overline{\mathbf{B}} + \overline{\tilde{\mathbf{A}} \cdot \tilde{\mathbf{B}}}, \tag{18}$$

$$\tilde{\chi}^{(tot)} = \tilde{\chi} + \overline{\mathbf{A}} \cdot \tilde{\mathbf{B}} + \tilde{\mathbf{A}} \cdot \overline{\mathbf{B}} + \tilde{\mathbf{A}} \cdot \tilde{\mathbf{B}}, \tag{19}$$

Evolution of the $\overline{\chi}$ and $\tilde{\chi}$ is governed by the corresponding parts of Eq(17). The magnetic helicity conservation is determined by the magnetic Reynolds number R_m. In this paper we employ $R_m = 10^6$. Note, that the nonaxisymmetric $\tilde{\alpha}$ in the sum of

the Eq(15), like the $\overline{\alpha}$, follows the mean field analytical expression,

$$\tilde{\alpha} \quad = \quad C_\alpha \psi_\alpha(\tilde{\beta}) \alpha_{\phi\phi}^{(H)} + \alpha_{\phi\phi}^{(M)} \psi_\alpha(\tilde{\beta}) \frac{(\overline{\chi} + \tilde{\chi})\, \tau_c}{4\pi \overline{\rho} \ell_c^2}, \tag{20}$$

where $\tilde{\beta} = \left|\tilde{\boldsymbol{B}}\right| / \sqrt{4\pi \overline{\rho} \mathrm{u}_c^2}$ is nonaxisymmetric measure of the local magnetic field strength.

In our paper, we investigate the relative contributions of the Eq.(15) to the large-scale dynamo. The rest of the model is devoted to the solution of the mean-field heat transport and angular momentum balance in the solar convection zone. This part of the model was described in Pipin & Kosovichev (2020). We employ the stellar interior model MESA (Paxton et al. 2011, 2013) to define the reference profiles of mean thermodynamic parameters, such as entropy, density, temperature and the convective turnover time, τ_c. We assume that τ_c does not depend on evolution of the magnetic field and global flows. The convective RMS velocity u_c is defined via the mixing-length approximation,

$$\mathrm{u_c} = \frac{\ell_\mathrm{c}}{2} \sqrt{-\frac{\mathrm{g}}{2\mathrm{c_p}} \frac{\partial \overline{\mathrm{s}}}{\partial \mathrm{r}}}, \tag{21}$$

where $\ell_c = \alpha_{MLT} H_p$ is the mixing length, $\alpha_{MLT} = 1.9$ is the mixing length parameter, and H_p is the pressure height scale. The Eq. (21) defines the profiles of the eddy heat conductivity, χ_T, eddy viscosity, ν_T, and eddy diffusivity, η_T, as follows,

$$\chi_T \quad = \quad \frac{\ell^2}{6} \sqrt{-\frac{g}{2c_p} \frac{\partial \overline{s}}{\partial r}}, \tag{22}$$

$$\nu_T \quad = \quad \mathrm{Pr}_T \chi_T, \tag{23}$$

$$\eta_T \quad = \quad \mathrm{Pm_T} \nu_\mathrm{T}. \tag{24}$$

The model shows the agreement of the angular velocity profile with helioseismology results for $\mathrm{Pr}_T = 3/4$. Also, the dynamo model reproduces the solar cycle period, ~ 22 years, if $\mathrm{Pm}_T = 10$ and $C_\alpha = 0.04$. The level C_α is slightly above of the critical threshold.

The integration domain is divided into two parts. The overshoot region includes the part of the radiative zone. The bottom of the integration domain is fixed at $r = 0.68$R. The convection zone extends from $r = 0.728R$ to $0.99R$. The solution of the heat transport gives the mean entropy distribution and determines the turbulent parameters in the convection zone. In the overshoot region the intensity of the turbulent mixing decay exponentially from the bottom of the convection zone. The solid-body rotation of the rate $\Omega_0 = 433$Nhz is applied at the low boundary ($r = 0.68$R). We put the strength of the magnetic field component there to zero. At the top boundary, ($r = 0.99$R) we use the black-body radiation heat flux and the stress-free condition for the hydrodynamic part of the problem. Like Moss & Brandenburg (1992); Rüdiger et al. (2018); Pipin & Kosovichev (2019), we use a combination of the superconductor and insulator boundary conditions for the axisymmetric toroidal field at the top of the domain (see, Pipin & Kosovichev 2019). The poloidal magnetic field, as well as the nonaxisymmetric parts of the large-scale magnetic field, extends outside following the potential magnetic field distribution with the source surface at $r = 2.5R$ (Hoeksema 1984).

The nonaxisymmetric part of the dynamo model was solved using the spherical harmonics. For this problem, we employ the FORTRAN version of the SHTNS library of Schaeffer (2013). For the MESA convection zone parameters we find the maximum magnitude of the magnetic buoyancy velocity at the extrema points is about factor 3-5 less than the convective RMS velocity in the upper part of the convection zone, i.e., $V_\beta\,(r_m, \theta_m) \approx$30-50 m/s.

The Figure1 shows the angular velocity profile, streamlines of the meridional circulation, the radial profiles of the α - effect and the eddy diffusivity in the model. The magnitude of the meridional flow on the surface is about 13 m/s. The angular velocity profile agrees well with helioseismology data. A discussion of the mechanisms generating the differential rotation and meridional circulation in our model can be found in Pipin & Kosovichev (2018) (and for further explanations, also, see, Kitchatinov & Rüdiger 1999, 2005).

The Figure 2 shows the magnetic field distribution that results from the BMRs formation from the background axisymmetric magnetic field. We see that inside the star the magnetic field is mostly axisymmetric. The nonaxisymmetric part of the magnetic field is shallow. Also, by design, the magnetic buoyancy instability operates above $0.85R$ (see, comments below the Eq8). The instability condition, which is given by the Eq(9), shows the most unstable part of the toroidal magnetic field is located at the equatorial edge of the dynamo wave. For this illustration we loosely use the negative α_β in the northern hemisphere which is opposite to the theoretically expected sign of the α-effect. Note that the northern BMR shows the negative tilt. The southern BMR follows to the Joy's law as we impose the negative α-effect for it. The Figure 2shows that the nonaxisymmetric magnetic field is rather shallow. The weak nonaxisymmetric field of the few Gauss strength is present in the depth of the convection zone. Its effect on the dynamo there is negligible in comparison to the axisymmetric toroidal magnetic field. At the top, the situation is the opposite. The model takes into account the effects of the magnetic field on the *axisymmetric* flow and heat transport in the convection zone. The nonaxisymmetric effect in the hydrodynamic part of the model has to be developed further in the way drew by Moss et al. (1991). The emerging BMRs affect the solar cycle variations of the angular velocity and

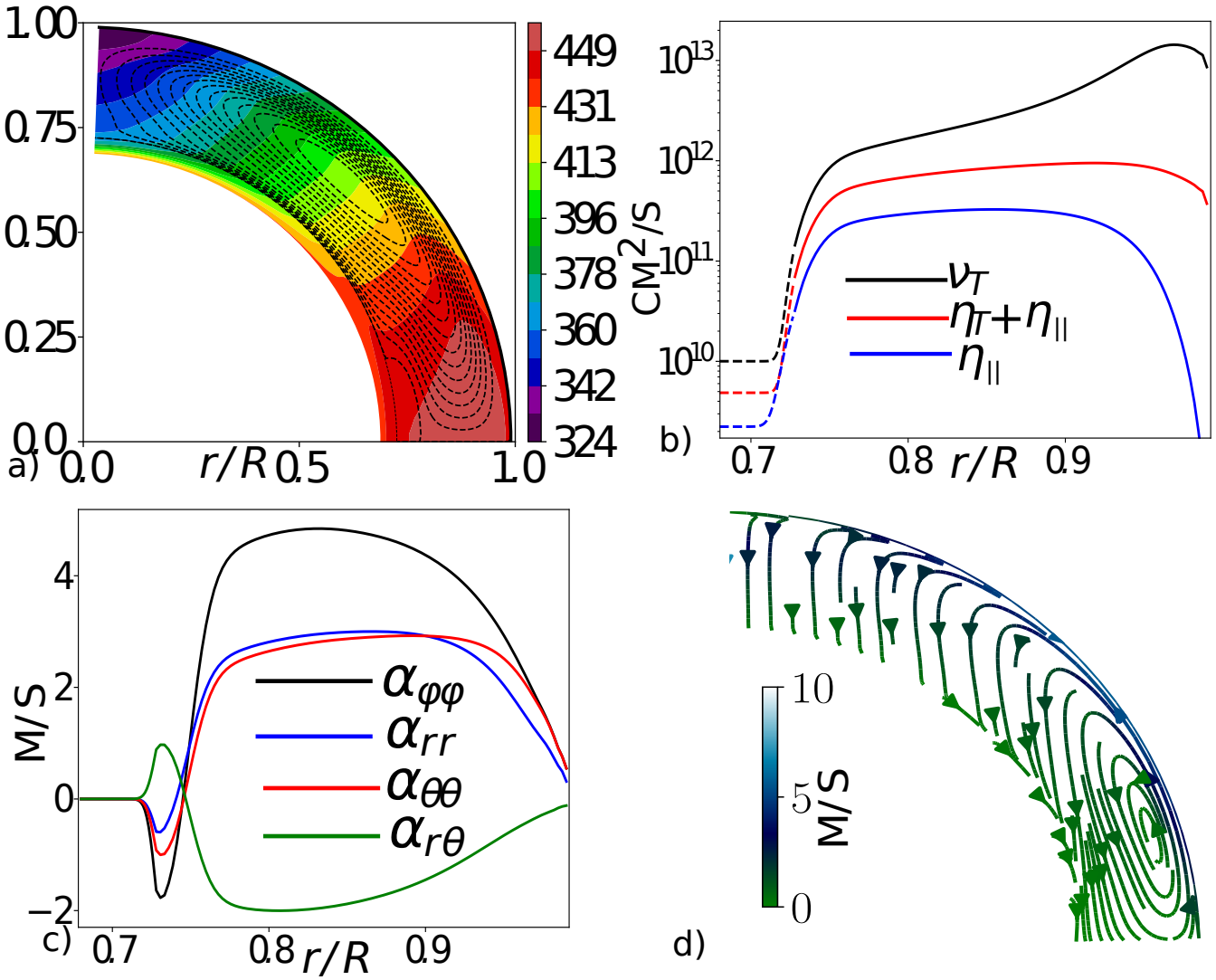

Figure 1. a) The reference angular velocity profile (linear case) and the streamlines of the meridional circulation with the maximum circulation velocity of 13 m/s on the surface at the latitude of 45°; b) radial profiles of the total, $\eta_T + \eta_{||}$, and the rotationally induced part, $\eta_{||}$, of the eddy magnetic diffusivity and the eddy viscosity profile; c) radial profiles of the α-effect tensor at the latitude of 45°; and d) the streamlines of the effective velocity due to the meridional circulation and the turbulent pumping effect. Here, and below we use NUMPY/SCIPY (Harris et al. 2020; Virtanen et al. 2020) together with MATPLOTLIB (HUNTER 2007) and PYVISTA (SULLIVAN & KASZYNSKI 2019) for post-processing and visualization.

the meridional circulation (Komm et al. (2015); Howe et al. (2018); Kosovichev & Pipin (2019); Getling et al. (2021)). The discussion of these effects is postponed to another paper.

3 RESULTS

The Figure 3 shows the time-latitude diagram of the axisymmetric magnetic field evolution in the model. The results are similar to those presented in our previous papers (see, Pipin & Kosovichev (2019); Obridko et al. (2021)). In the mid-latitudes, the radial magnetic field shows an intermittent surge-like pattern. It results from contributions of the weak diffuse field of the large-scale dynamo and remnants of the BMRs decay. A similar pattern is found in the surface flux transport models and 3d Babcock-Leighton types models (e.g., Mackay & Yeates 2012; Hazra & Nandy 2019; Kumar et al. 2019). Notably, the intermittency of the flux in our model is higher than that in the above-cited paper of Kumar et al(2019). This is probably due to the larger size of the active regions in our case.

Starting our simulations from the same initial conditions we compare two runs of the model with and without BMR emergence. Figure 3c shows the evolution of the total unsigned flux of the axisymmetric toroidal magnetic field in the convection zone. The parameters of the runs diverge with time because the dynamo period is different in these two cases. Similar to Obridko et al.

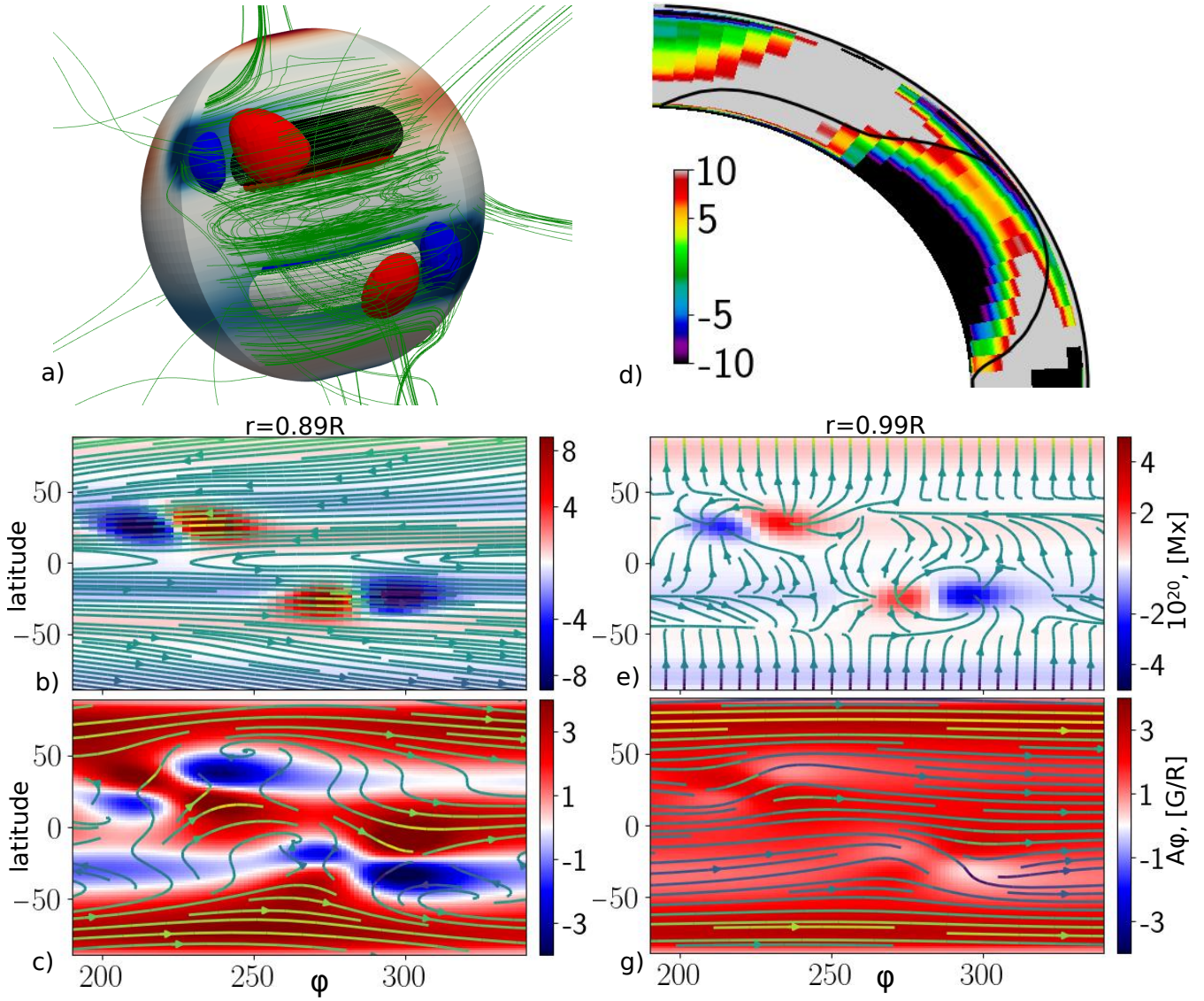

Figure 2. a) Magnetic field distribution inside and above the star after the BMR injection: red and blue colors show the radial magnetic field flux range of $\pm 10^{21}$Mx, separately we show the magnetic flux islands with pixels of $\pm 3 \cdot 10^{20}$Mx; black and white colors show the tors of the azimuthal magnetic field of the strength $\pm$1.5kG inside the convection zone; the magnetic field lines are shown in green color; b) snapshot of the magnetic instability parameter I in the northern hemisphere; c) Synoptic map of the magnetic field distribution at the level r=0.89R, the color image shows the radial magnetic field flux in range of $\pm 10^{21}$Mx and streamlines show the horizontal magnetic field; d) color shows the azimuthal magnetic vector-potential,$\langle A_\varphi \rangle$, and streamlines show the horizontal magnetic vector-potential field; e) and g) show the same for the top boundary.

(2021), we see that the model with BMRs shows a smaller period than the model without BMRs. This is due to the additional generation effect from the BMRs evolution. Also, we see that the full model shows the decrease of the toroidal magnetic flux oscillations. This effect results from the additional magnetic flux loss through the BMRs emergence. From the results of Figs.3b and c we see that the amount in the convection zone exceed 10^{24} Mx. Also, the flux generated by the BMRs is larger than the oscillation magnitude of the toroidal magnetic field flux. The present 3D model is not fully self-consistent. Indeed, the energy for the BMR instability should be taken from somewhere, e.g., from the energy of the convective flows. Meantime, the evolution of the axisymmetric dynamo in the model is self-consistent with the large-scale flow and heat transport in the convection zone.

The Figure 4 shows snapshots of the radial magnetic field flux at the surface and the magnetic field distribution inside the convection zone during the maximum of the magnetic cycle at the time around 30yr. At the low latitudes of the star, the magnetic field is fairly nonaxisymmetric in the shallow layer below the surface. The differential stretches the toroidal field toward the poles from the nonaxisymmetric remnants of the large unipolar magnetic regions. In general, we find that our model fairly well reproduces the magnetic flux evolution on the solar surface in qualitative agreement with solar observations (e.g., Giovanelli 1985; Wang et al. 1989; Virtanen et al. 2019).

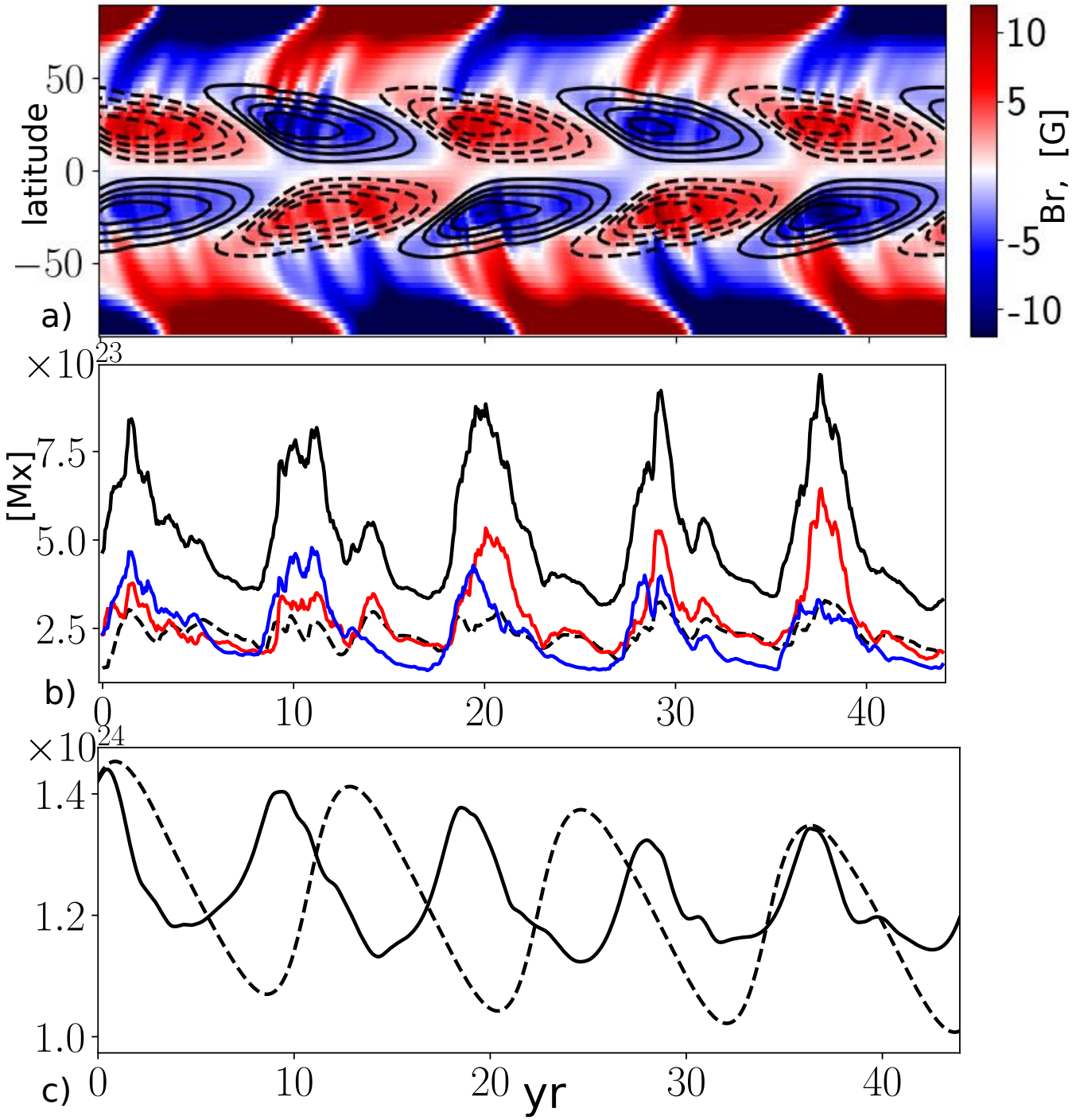

Figure 3. a) The time-latitude diagram of the subsurface axisymmetric toroidal magnetic field (contours of range ±1kG at r=0.9R and the surface radial magnetic field; b) the total unsigned flux of the radial magnetic field (black line), the blue and red lines show the same for the northern and southern hemispheres, respectively, the dashed line shows the flux of the axisymmetric radial magnetic field; c) Evolution of the total flux of the axisymmetric toroidal magnetic field in the convection zone in the model with BMRs emergence (solid line) and without it (dashed line);

3.1 Zonal harmonics

The mean field expressions for the $\overline{\alpha}$ and $\tilde{\alpha}$ coefficients contain contributions of the kinetic and magnetic helicity, see, the Eqs(16,20). In this study we will distinguish the kinetic and magnetic part of the α effect only in the axisymmetric coefficient $\overline{\alpha}$. The mean electromotive force for the large-scale axisymmetric poloidal magnetic field generation reads as follows,

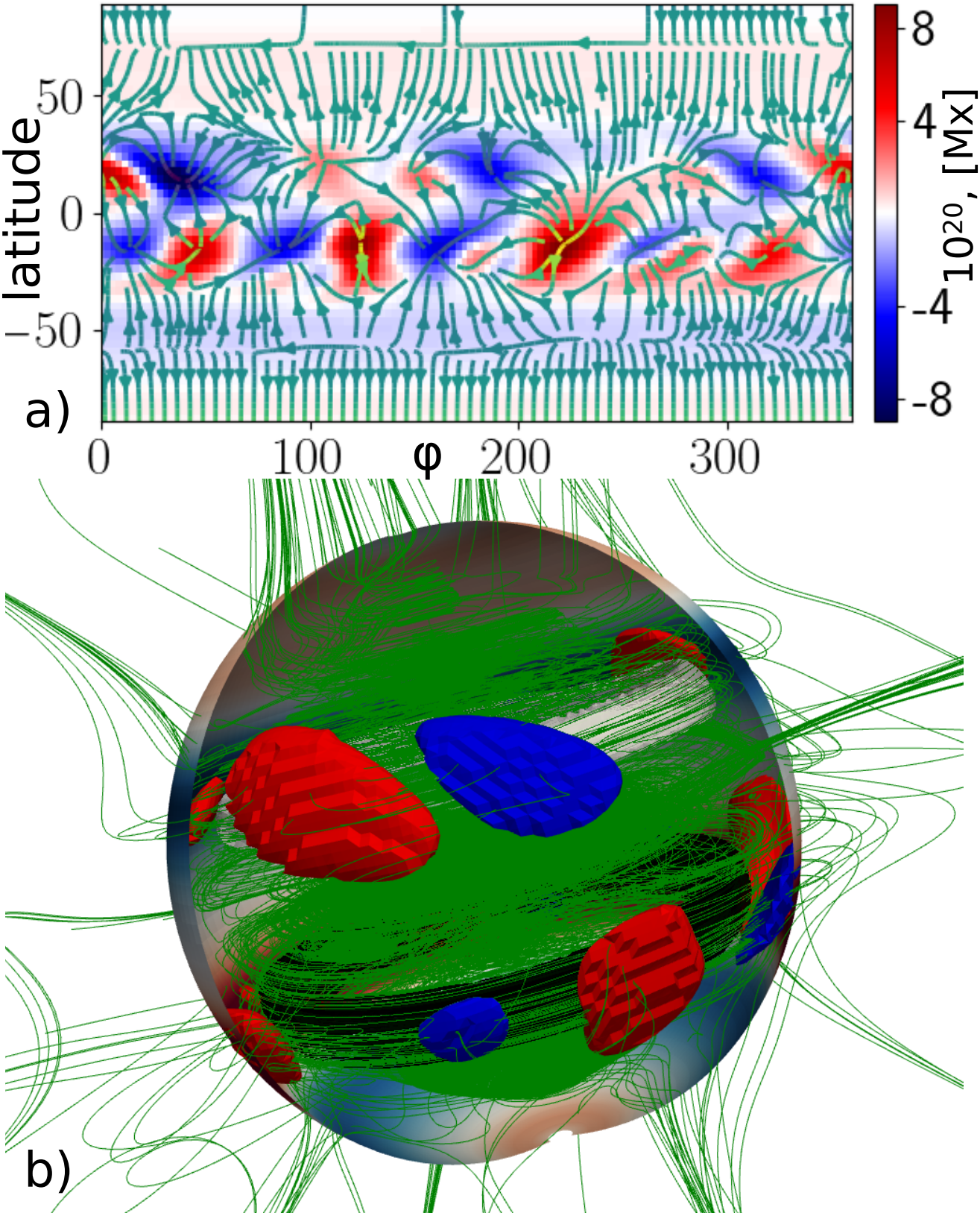

Figure 4. The same as Figc.2a) and g) for the magnetic field distribution during the magnetic cycle maximum at the time around 30 yr.

$$\mathcal{E}^{\alpha}_{\phi} = \left(\overline{\alpha}^{(H)} + \overline{\alpha}^{(M)}\right) B + \overline{\tilde{\alpha}\tilde{B}_{\phi}} + \overline{\alpha_{\beta} \langle B \rangle_{\phi}}, \tag{25}$$

$$\equiv E_1 + E_2 + E_3 + E_4 \tag{26}$$

where the sum in the first term in the RHS corresponds to the Eq(16), and $E_{\{n\}}$ denotes the corresponding terms in the Eq(16), e.g., $E_2 \equiv \overline{\alpha}^{(M)} B$. Obridko et al. (2021) found that the zonal harmonics are useful to distinguish between effects of the deep and surface magnetic field generation. This is because of the phase difference between the zonal harmonics of different ℓ (Stenflo 1994).

Following this idea, in Figure we show results for the first three *odd* harmonics ($\ell = 1, 3, 5$) of the radial magnetic field at the surface and the first three *even* harmonics ($\ell = 0, 2, 4$) of the mean electromotive force parameters $E_{\{n\}}$ at the near-surface level r=0.987R. These even harmonics correspond to the time derivative of the vector-potential (see, the Eq(13)), and they are readily connected to the odd harmonics of the axisymmetric radial magnetic field. The evolution of the ℓ-harmonics of the radial magnetic field is in agreement with observations. The phases of the ℓ_1 and ℓ_3 are closer to each other than the axisymmetric dynamo model shows. This is the effect of the BMR emergence and evolution (Obridko et al. 2021). In addition, Fig.5a shows the results of the model run without BMR. We see that the magnitude of the modes ℓ_3 and ℓ_5 is larger when the effect of BMRs is included. In addition, we find the generation of the ℓ_2 harmonic in the full model. This mode is generated solely due to fluctuations of the BMR's tilt, which are due to the randomness of the α_{β}. Similar results were found by Hazra & Nandy (2019). In excluding the random α_{β}, we got no generation of the ℓ_2 harmonic. The same is found for the model without BMRs (see, Fig.5a).

The phases of the $E_1^{(0)}(\ell = 0)$, as well as, this harmonic of the total $\mathcal{E}^{\alpha}_{\phi}$, are shifted by $\pi/2$ of the $\overline{B_r}^{(1)}$ evolution. The higher modes do not show this because of the mode mixing. The magnetic helicity alpha effect, $E_2^{(0)}$, shows the oscillation with about twice as high frequency of the $E_1^{(0)}$. We found that $E_2^{(0)}$ has opposite sign to $E_1^{(0)}$ during the maximum of the magnetic activity. This corresponds to the magnetic helicity quenching effect (see, Kleeorin & Ruzmaikin 1982; Kleeorin & Rogachevskii 1999; Brandenburg 2018). The $\ell = 0$ α effect generation from the BMR emergence, $E_4^{(0)}$, show spikes, which sign in average corresponds to the sign of $E_1^{(0)}$ (by definition). The sum of $E_3 + E_4$ show the long-term variations which result from the cumulative α effect generation from the tilted BMR emergence and the nonaxisymmetric azimuthal component of the magnetic field. The latter results from the BMRs evolution due to effects of the large-scale flow (e.g., differential rotation and meridional circulation) and turbulent diffusion. The $\ell = 4$ harmonics of the $\mathcal{E}^{\alpha}_{\phi}$ show the qualitatively similar evolution as the $\ell = 0$ harmonics. The behavior of the $\ell = 2$ harmonic is different. This harmonic is the primary source of the $\ell = 3$ harmonic of the radial magnetic field. Interesting that the $\ell = 2$ contributions of $E_1$and E_2 go in phase in such a way that the magnetic helicity increase the magnetic field generation produced by the kinetic α effect. From Fig.5c we see that the $\ell = 2$ harmonic of E_2 show the 5-year oscillations modulated by a 20-year magnetic cycle. Note, that the $\ell = 2$ harmonic of E_2shows the 2-year oscillations, see Fig.5d.

The ℓ - harmonics of the total contribution of the α effect magnetic field generation, $\mathcal{E}^{\alpha}_{\phi}$, at the near-surface layer are shown in Fig.6a. We see the considerable effect of the surface BMRs on the magnetic field generation. This effect decreases rapidly with the depth, see Fig.6b. In our model, the near-surface nonaxisymmetric magnetic field does not penetrate deep in the convection zone. Therefore in the deep layers, the effect of the BMR emergence is only due to perturbations that are produced by the spikes due to the magnetic buoyancy effects. Interesting, that the ℓ_1 mode of $\mathcal{E}^{\alpha}_{\phi}$, which is responsible for generation of the even parity poloidal magnetic field, penetrates deep in the convection zone. Therefore, the fluctuations of the surface BMRs tilt can result to the parity breaking in the whole dynamo operating in the bulk of the convection zone.

3.2 Magnetic helicity evolution

Results of the previous subsection show the interesting features of the mean electromotive force due to the magnetic helicity effects. As the first step, we look at the effect of the BMR emergence on the surface magnetic helicity distribution. It is illustrated in Fig.7. The synoptic maps show the situation after the polar field reversal at the time step around 10 years. Similar, to the result of Yeates (2020); Pipin (2021), we find that emergence of the BMR in the ambient large-scale field injects the magnetic helicity at the same place. The effect results from the magnetic helicity conservation. In the dynamo, like that which is assumed to be operating in the Sun, the axisymmetric magnetic field satisfies the hemispheric rule with the positive magnetic helicity in the northern hemisphere and opposite in the southern one (Blackman & Brandenburg 2003). The emerging BMR results in the globally bihelical structure. Figs.7a and b show the snapshots of the surface magnetic field and vector-potential at the time around of the activity maximum. In the place of the flux emergence, the helicity density distribution shows the areas of the opposite sign with the nearly zero integral balance. In particular, it is well seen in the case of the new BMR in the southern hemisphere at about 230 degrees longitude. This BMR shows the quadrupolar helicity density structure. The evolved BMR shows the increase of the helicity density sign of one polarity. The sign is opposite to the hemispheric rule for the large-scale field. For example, in the North, we see the BMR at 150-degree longitude with the dominant-negative helicity

density and at the South - the opposite situation for the BMR at 90-degree longitude. The position of maximum corresponds to the neutral line between the opposite BMR polarities. Its equator to poles elongation results from the BMR evolution due to the differential rotation. The helicity injection due to the differential rotation was recently discussed by Hawkes & Yeates (2019) using the surface flux transport model. Fig7b shows the generation of the azimuthal vector-potential inside the evolved BMR. The sign of the generated vector-potential is opposite to that which is generated by the α effect in the new tilted BMRs. To see this we can confront the evolved and new BMRs in the southern hemisphere. The effect of the injected helicity in the evolved BMRs on the dynamo is small because of the total helicity balance. The polar sides of the synoptic maps show the large-scale field helicity density satisfies the hemispheric sign rule, i.e., it has a positive sign in the northern hemisphere. The longitudinally averaged synoptic map Fig7c shows extrema of the opposite hemispheric sign rule, i.e., negative at the North and positive at the South. In each hemisphere, the imbalance of the total helicity is more than order of magnitude less than those extrema in Fig7d (cf, Yeates 2020).

Fig.8 shows results of the model for the time-latitude evolution of the toroidal magnetic field in the subsurface layer and the magnetic helicity evolution. The results for the total magnetic helicity (Fig.8a) are in the qualitative agreement with the solar observation (see, e.g., Lund et al. 2020 and Pevtsov et al. 2021). The evolution of the small-scale helicity density, $\langle\chi\rangle$, which is produced by the dynamo follows the Eq(17). The model shows the $\langle\chi\rangle$ time-latitude diagram at the near-surface layer in general agreement with the results of our previous papers and we do not show it here (see, e.g, Pipin et al. 2013; Pipin 2018). Instead, the rather interesting question is about the helicity density evolution of the large-scale nonaxisymmetric magnetic field. Fig.8b show the time-latitude evolution of the $\overline{\tilde{\mathbf{A}}\cdot\tilde{\mathbf{B}}}$ and similar diagram for the axisymmetric magnetic field helicity density, i.e., $\overline{\mathbf{A}}\cdot\overline{\mathbf{B}}$. The $\overline{\tilde{\mathbf{A}}\cdot\tilde{\mathbf{B}}}$ show the good agreement with the results of Pipin et al. (2019), who measured the helicity density using the synoptic maps of SDO/HMI. We see that the helicity density $\overline{\tilde{\mathbf{A}}\cdot\tilde{\mathbf{B}}}$ shows the predominantly negative sign in the northern hemisphere and opposite sign in the southern hemisphere. This is in agreement with the hemispheric sign rule (HSR) for the current helicity of the solar active regions (Seehafer 1990; Pevtsov et al. 1994; Bao et al. 2000; Zhang et al. 2010). The magnetic field, which is involved in the $\overline{\tilde{\mathbf{A}}\cdot\tilde{\mathbf{B}}}$ occupies the intermediate spatial scales. On the surface, the axisymmetric magnetic field shows variations of the helicity density sign from the negative in the northern hemisphere during the minimum of the magnetic cycle to the positive during the maximum cycle. In the southern hemisphere, the $\overline{\mathbf{A}}\cdot\overline{\mathbf{B}}$ evolves in the opposite way. A very similar pattern is found in the solar observations (Pevtsov et al. 2021).

The theoretical expectation suggests the bihelical magnetic field in the large-scale dynamo (Blackman & Brandenburg (2003); Brandenburg (2018); Brandenburg et al. (2017)). The large-scale magnetic field is assumed to have the positive helicity sign and the small-scale fields have the opposite sign of the magnetic helicity. The direct computation of the helicity spectrum from distributions of the vector-potential and magnetic field has two issues. It depends on the gauge of the vector potential. Another issue is that the different ℓ harmonics of the magnetic helicity density may not show the same hemispheric sign rule. The two-scale approach of Roberts & Soward (1975) was suggested and developed (see, Brandenburg et al. (2017); Brandenburg (2019); Prabhu et al. (2021)) to overcome the issues. As the first try, we calculate the helicity proxy spectrum suggested by Brandenburg (2019). The proxy is determined by the spherical harmonics of the superpotentials S and T (see, 4) as follows

$$H_{\ell}^{\pm} = \sum_{m=-\ell}^{m=\ell} 2\ell\,(\ell+1)\,S_{\ell\,m}T^{*}_{\ell\pm1\,m}, \tag{27}$$

where the shift $\ell\pm1$ was introduced to account for the two-scale approximation. By definition, the $H_{\ell}^{\pm}$ should have the positive sign at the low ℓ in correspondence of the conventional hemispheric sign rule, i.e., the predominantly positive helicity for the large-scale magnetic field in the northern hemisphere. Fig.8c shows the evolution of the H_{ℓ}^{+} at the surface. The general sign of H_{ℓ}^{+} is in agreement with the helicity density evolution shown in Figs8a and b. It is opposite to the theoretical expectation. Yet, the ℓ_1 mode shows the positive sign in agreement with the large-scale helicity density on the synoptic maps of the Fig.7. We also calculated the H_{ℓ}^{+} for the depth of the subsurface shear layer, at r=0.9R. There the sign of H_{ℓ}^{+} is in agreement with expectations. The sign of the ℓ_1 mode does not show the change. Derivation of the Eq.(27) employs the potential boundary condition for the S. Therefore its interpretation for the depth of the convection zone can be biased. We find that the patterns of $H_{\ell}^{-}$are very similar to H_{ℓ}^{+}. It would be interesting to calculate the helicity spectrum from the Gauss linking formula (see, Moffat 1969; Berger 1984 and Prabhu et al. 2021). We postpone this for future studies.

4 DISCUSSION AND CONCLUSIONS

The dynamo model, which is presented in the paper, combines the framework of the mean-field dynamo and phenomenological parts of the Babcock-Leighton scenarios. Similar work was presented earlier in the papers by Passos et al. (2014); Kumar et al. (2019). In our model the phenomenology of the BMR formation was formulated using the mean electromotive force with the addition of the magnetic buoyancy effect for the nonaxisymmetric magnetic field. The tilt of the BMR is introduced by the α

effect acting on the buoyantly unstable part of the magnetic field. The parameters of the phenomenological part were chosen to fit observations of the solar BMRs.

To study how much the surface magnetic activity can affect the dynamo generation we compare the α effect contributions of the BMRs with the same terms of the axisymmetric large-scale field, see the Eq(25). The emergence of the tilted bipoles produces two dynamo effects into the azimuthal electromotive force, E_3 and E_4. The latter results from the tilt of the BMRs. It shows the spike-like evolution. The E_4 of the individual region goes to zero after the region initiation. The E_3 produces the long-term dynamo contribution of the BMR by means of the standard α effect. Still, the amplitude of the initial tilt is important for the long-term generation effect by means of E_3. This was confirmed by additional runs with $E_4 \equiv 0$. At the surface, the dynamo effect of the BMRs is stronger than the mean-field generation effects. In comparison to the Babcock-Leighton dynamos, the effect of the surface magnetic activity on the dynamo in the convection zone is not strong. This is because the nonaxisymmetric magnetic field is shallow. The main source of the nonaxisymmetric magnetic field is the BMR formation and evolution at the surface. Note, the strong differential rotation of the Sun does not support the dynamo instability of the nonaxisymmetric magnetic field. The weak nonaxisymmetric field can be excited due to the nonlinear effects (Moss 1999) or the nonaxisymmetric perturbations of the α effect (Bigazzi & Ruzmaikin 2004). The most important consequence of the surface BMR evolution is breaking the reflection symmetry of the large-scale magnetic field about the equator. The effect is caused by the random fluctuations of the tilt of the BMRs. It was discussed recently by Hazra & Nandy (2019) in the context of the long-term parity variations in the solar dynamo. The study of the parity-breaking mechanisms in the solar dynamo has a long history (Ivanova & Ruzmaikin 1976; Brandenburg et al. 1989; Sokoloff & Nesme-Ribes 1994; Knobloch et al. 1998; Weiss & Tobias 2016). We can explain the global effect of the surface BMRs' tilt fluctuations on the dynamo if we take into account that the even parity dynamo modes are close (and still below) to the dynamo instability threshold. To see the prospect of this mechanism in our dynamo model we have to make the longer simulation runs.

The magnetic helicity contributions to the α effect reveal interesting properties which can be connected to the origin of the short-term oscillations of the large-scale magnetic field. We have seen that the quenching of the dynamo generation by means of the magnetic helicity acts differently on the different ℓ-modes of the large-scale magnetic fields. In particular, The $\hat{\ell}_0$ mode of the magnetic helicity α effect reveals the 5-year oscillations. This mode suppresses the generation of the polar dipole during the maximum of the magnetic cycle. Its frequency is defined by the nonlinear B^2 generation of the small-scale magnetic helicity in the presence of the large-scale magnetic field. These 5-year oscillations affect the shape of the dipole mode oscillation of the radial magnetic field (Sokoloff et al. (2020)). The ℓ_2 and ℓ_4 show oscillations of short periods between 2 and 3 years. Remarkably, instead of quenching the ℓ_2 mode of the magnetic helicity α effect support generation of the polar octupole. The ℓ_4 mode shows the quasi-biennial oscillations. The quenching mechanism due to this mode results in the dispersion of the signal of the main generation effect due to the kinetic part of the α effect. The emerging BMRs result to the random fluctuation of the mean-field generation effect. The mean sign and magnitude of these fluctuations correspond to the sign and magnitude of the kinetic α effect. This partly follows from the design of the phenomenological part of the model. The above discussion shows the particular importance of the mean-field evolution of the bipolar active regions for the results of the model.

The model allows us to study the effects of the BMR on the surface magnetic helicity evolution. This is important both for interpretation of the solar observation and understanding what part of the observed magnetic helicity comes from the near-surface effects and from the dynamo deep in the convection zone. As was discussed by Yeates (2020), the emerged BMRs result in the surface helicity density distributions with nearly zero integral imbalance. Therefore, the magnetic helicity α effect of these BMRs on the large-scale dynamo is about zero. The results in Fig8 show that on the surface the effects of the helicity contributions which come from the large-scale dynamo are contaminated by the helicity injection due to the BMR emergence. We see that using observations of the surface helicity density evolution it may be difficult to distinguish the helicity contributions that crucial for the global dynamo. The model shows that the hemispheric sign rule of the large-scale nonaxisymmetric magnetic field helicity density corresponds to the expected sign rule of the small-scale magnetic field helicity density, i.e., the $\overline{\tilde{\mathbf{A}} \cdot \tilde{\mathbf{B}}}$ has the negative sign in the northern hemisphere. As noted by Prabhu et al. (2021), Pipin et al. (2019) misinterpreted the $\overline{\tilde{\mathbf{A}} \cdot \tilde{\mathbf{B}}}$ as the small-scale helicity density. The two-scale approach of Brandenburg et al. (2017); Brandenburg (2019); Prabhu et al. (2021) to infer the spectral properties of the of magnetic helicity in the large-scale dynamo is consistent with the mean-field MHD framework. We try the proxy parameter suggested by Brandenburg (2019). Indeed, the proxy shows the two-scale spectrum (see, Fig8c) with positive helicity sign at very low ℓ for the northern hemisphere of the star. The rest of the spectrum shows the negative helicity sign. This is of course, due to the negative helicity density in the evolved BMRs in the northern hemisphere. Note that our approach to model the surface activity is very simple. It excludes the complicated processes which are involved in the formation of the solar active regions. Nevertheless, our results shed some light on the fluctuations of the hemispheric sign rule in the bihelical helicity spectra of the solar magnetic field as was reported by Singh et al. (2018). The two-scale method relies on the bihelical magnetic helicity spectrum which results from redistribution of the magnetic helicity over the spatial scales due to the dynamo action and the magnetic helicity conservation (Frisch et al. 1975; Pouquet et al. 1975; Kleeorin & Ruzmaikin 1982). Yet, most part of the nonaxisymmetric magnetic field on the solar surface is generated due to the BMR emergence and evolution. Raedler (1986) noted that the properties of this field are different from

those generated by the global dynamo. This should be taken into account in the interpretation of the solar/stellar observations of the magnetic helicity.

Finally, I would like to summarize the main results of the study as follows. We investigate the effect of the tilted bipolar magnetic regions (BMR) emergence on the large-scale dynamo distributed in the bulk of the convection zone. The BMR effects are restricted to the shallow layer occupying the depth of the subsurface shear layer. At the surface the effect of the BMR on the magnetic field generation is dominant. However, because of the shallow BMR distribution, its effect on the global dynamo is moderate. The most dynamo effect of the surface BMR rises due to their evolution and the convective zone α effect. The fluctuations of the BMR's tilt affect the equatorial symmetry parity. The suggested model is quite simple. The straightforward generalization is to take the 3D effect of the large-scale flow into account.

REFERENCES

Acheson D. J., Gibbons M. P., 1978, Journal of Fluid Mechanics, 85, 743
Babcock H. W., 1961, ApJ, 133, 572
Bao S. D., Ai G. X., Zhang H. Q., 2000, Journal of Astrophysics and Astronomy, 21, 303
Berger Mitchell A.; Field G. B., 1984, Journal of Fluid Mechanics, 147
Berger M. A., Hornig G., 2018, Journal of Physics A Mathematical General, 51, 495501
Bigazzi A., Ruzmaikin A., 2004, ApJ, 604, 944
Blackman E. G., Brandenburg A., 2003, ApJ, 584, L99
Bonanno A., 2016, ApJ, 833, L22
Brandenburg A., 2018, Journal of Plasma Physics, 84, 735840404
Brandenburg A., 2019, ApJ, 883, 119
Brandenburg A., Krause F., Meinel R., Moss D., Tuominen I., 1989, A&A, 213, 411
Brandenburg A., Kleeorin N., Rogachevskii I., 2013, ApJ, 776, L23
Brandenburg A., Petrie G. J. D., Singh N. K., 2017, ApJ, 836, 21
Brun A., Garcia R., Houdek G., Nandy D., Pinsonneault M., 2014, Space Science Reviews, pp 1–54
Cameron R. H., Schüssler M., 2017, A&A, 599, A52
Davies C. R., Hughes D. W., 2011, ApJ, 727, 112
Frisch U., Pouquet A., Léorat J., A. M., 1975, J. Fluid Mech., 68, 769
Getling A. V., 2001, Astronomy Reports, 45, 569
Getling A. V., Kosovichev A. G., Zhao J., 2021, ApJ, 908, L50
Gilman P. A., 1970, ApJ, 162, 1019
Gilman P. A., 2018, ApJ, 867, 45
Giovanelli R. G., 1985, Australian Journal of Physics, 38, 1045
Hale G. E., Ellerman F., Nicholson S. B., Joy A. H., 1919, ApJ, 49, 153
Harris C. R., et al., 2020, Nature, 585, 357
Hathaway D. H., 2015, Living Reviews in Solar Physics, 12, 4
Hawkes G., Yeates A. R., 2019, A&A, 631, A138
Hazra S., Nandy D., 2019, MNRAS, 489, 4329
Hoeksema J. T., 1984, PhD thesis, Stanford Univ., CA.
Howe R., Hill F., Komm R., Chaplin W. J., Elsworth Y., Davies G. R., Schou J., Thompson M. J., 2018, ApJ, 862, L5
Hubbard A., Brandenburg A., 2012, ApJ, 748, 51
Hunter J. D., 2007, Computing in Science & Engineering, 9, 90
Ivanova T. S., Ruzmaikin A. A., 1976, Soviet Ast., 20, 227
Karak B. B., Jiang J., Miesch M. S., Charbonneau P., Choudhuri A. R., 2014, Space Sci. Rev., 186, 561
Kitchatinov L. L., Mazur M. V., 2000, Sol. Phys., 191, 325
Kitchatinov L. L., Pipin V. V., 1993, A&A, 274, 647
Kitchatinov L. L., Rüdiger G., 1999, A&A, 344, 911
Kitchatinov L. L., Rüdiger G., 2005, Astronomische Nachrichten, 326, 379
Kitchatinov L. L., Pipin V. V., Ruediger G., 1994, Astronomische Nachrichten, 315, 157
Kleeorin N., Rogachevskii I., 1999, Phys. Rev.E, 59, 6724
Kleeorin N. I., Ruzmaikin A. A., 1982, Magnetohydrodynamics, 18, 116
Kleeorin N. I., Rogachevskii I. V., Ruzmaikin A. A., 1989, Pis ma Astronomicheskii Zhurnal, 15, 639
Kleeorin N., Safiullin N., Kuzanyan K., Rogachevskii I., Tlatov A., Porshnev S., 2020, MNRAS, 495, 238
Knobloch E., Tobias S. M., Weiss N. O., 1998, MNRAS, 297, 1123
Komm R., González Hernández I., Howe R., Hill F., 2015, Sol. Phys., 290, 3113
Kosovichev A. G., Pipin V. V., 2019, ApJ, 871, L20
Krause F., Rädler K.-H., 1980, Mean-Field Magnetohydrodynamics and Dynamo Theory. Berlin: Akademie-Verlag
Kumar R., Jouve L., Nandy D., 2019, A&A, 623, A54
Leighton R. B., 1964, ApJ, 140, 1547
Losada I. R., Warnecke J., Glogowski K., Roth M., Brandenburg A., Kleeorin N., Rogachevskii I., 2017, in Vargas Domínguez S., Kosovichev A. G., Antolin P., Harra L., eds, IAU Symposium Vol. 327, Fine Structure and Dynamics of the Solar Atmosphere. pp 46–59 (arXiv:1704.04062), doi:10.1017/S1743921317004306
Lund K., et al., 2020, MNRAS, 493, 1003
Mackay D. H., Yeates A. R., 2012, Living Reviews in Solar Physics, 9, 6

Mitra D., Candelaresi S., Chatterjee P., Tavakol R., Brandenburg A., 2010, Astronomische Nachrichten, 331, 130
Moffat H., 1969, J . Fluid Mech., 35, 117
Moffatt H. K., 1978, Magnetic Field Generation in Electrically Conducting Fluids. Cambridge, England: Cambridge University Press
Moss D., 1999, MNRAS, 306, 300
Moss D., Brandenburg A., 1992, A&A, 256, 371
Moss D., Tuominen I., Brandenburg A., 1991, A&A, 245, 129
Obridko V. N., Pipin V. V., Sokoloff D., Shibalova A. S., 2021, MNRAS, 504, 4990
Parker E. N., 1955a, ApJ, 121, 491
Parker E., 1955b, Astrophys. J., 122, 293
Parker E. N., 1979, Cosmical magnetic fields: Their origin and their activity. Oxford: Clarendon Press
Parker E. N., 1984, ApJ, 281, 839
Passos D., Nandy D., Hazra S., Lopes I., 2014, A&A, 563, A18
Paxton B., Bildsten L., Dotter A., Herwig F., Lesaffre P., Timmes F., 2011, ApJS, 192, 3
Paxton B., et al., 2013, ApJS, 208, 4
Petrie G. J. D., Petrovay K., Schatten K., 2014, Space Sci. Rev., 186, 325
Pevtsov A. A., Canfield R. C., Metcalf T. R., 1994, ApJ, 425, L117
Pevtsov A. A., Bertello L., Nagovitsyn Y. A., Tlatov A. G., Pipin V. V., 2021, Journal of Space Weather and Space Climate, 11, 4
Pipin V. V., 2008, Geophysical and Astrophysical Fluid Dynamics, 102, 21
Pipin V. V., 2018, Journal of Atmospheric and Solar-Terrestrial Physics, 179, 185
Pipin V. V., 2021, Journal of Plasma Physics, 87, 775870101
Pipin V. V., Kosovichev A. G., 2018, ApJ, 854, 67
Pipin V. V., Kosovichev A. G., 2019, ApJ, 887, 215
Pipin V. V., Kosovichev A. G., 2020, ApJ, 900, 26
Pipin V. V., Sokoloff D. D., Zhang H., Kuzanyan K. M., 2013, ApJ, 768, 46
Pipin V. V., Pevtsov A. A., Liu Y., Kosovichev A. G., 2019, ApJ, 877, L36
Pouquet A., Frisch U., Léorat J., 1975, J. Fluid Mech., 68, 769
Prabhu A. P., Singh N. K., Käpylä M. J., Lagg A., 2021, A&A, 654, A3
Raedler K.-H., 1986, Astronomische Nachrichten, 307, 89
Roberts P., Soward A., 1975, Astron. Nachr., 296, 49
Rüdiger G., Schultz M., Stefani F., Hollerbach R., 2018, Geophysical and Astrophysical Fluid Dynamics, 112, 301
Schaeffer N., 2013, Geochemistry, Geophysics, Geosystems, 14, 751
Schrinner M., 2011, A&A, 533, A108
Schrinner M., Petitdemange L., Dormy E., 2011, A&A, 530, A140
Seehafer N., 1990, Sol. Phys., 125, 219
Singh N. K., Käpylä M. J., Brandenburg A., Käpylä Petri J., Lagg A., Virtanen I., 2018, ApJ, 863, 182
Sokoloff D., Nesme-Ribes E., 1994, A&A, 288, 293
Sokoloff D. D., Shibalova A. S., Obridko V. N., Pipin V. V., 2020, MNRAS, 497, 4376
Stein R. F., Nordlund Å., 2012, ApJ, 753, L13
Stenflo J. O., 1994, in Rutten R. J., Schrijver C. J., eds, NATO Advanced Study Institute (ASI) Series C Vol. 433, Solar Surface Magnetism. p. 365
Stenflo J. O., 2013, A&ARv, 21, 66
Stenflo J. O., Kosovichev A. G., 2012, ApJ, 745, 129
Sullivan C. B., Kaszynski A., 2019, Journal of Open Source Software, 4, 1450
Tlatov A., Illarionov E., Sokoloff D., Pipin V., 2013, MNRAS, 432, 2975
Ugarte-Urra I., Upton L., Warren H. P., Hathaway D. H., 2015, ApJ, 815, 90
Vidotto A. A., Lehmann L. T., Jardine M., Pevtsov A. A., 2018, MNRAS, 480, 477
Virtanen I. I., Pevtsov A. A., Mursula K., 2019, A&A, 624, A73
Virtanen P., et al., 2020, Nature Methods, 17, 261
Wang Y. M., Nash A. G., Sheeley N. R. J., 1989, ApJ, 347, 529
Warnecke J., Rheinhardt M., Viviani M., Gent F. A., Tuomisto S., Käpylä M. J., 2021, ApJ, 919, L13
Weiss N. O., Tobias S. M., 2016, MNRAS, 456, 2654
Yeates A. R., 2020, ApJ, 898, L49
Yeates A. R., Nandy D., Mackay D. H., 2008, ApJ, 673, 544
Zhang H., Sakurai T., Pevtsov A., Gao Y., Xu H., Sokoloff D. D., Kuzanyan K., 2010, MNRAS, 402, L30

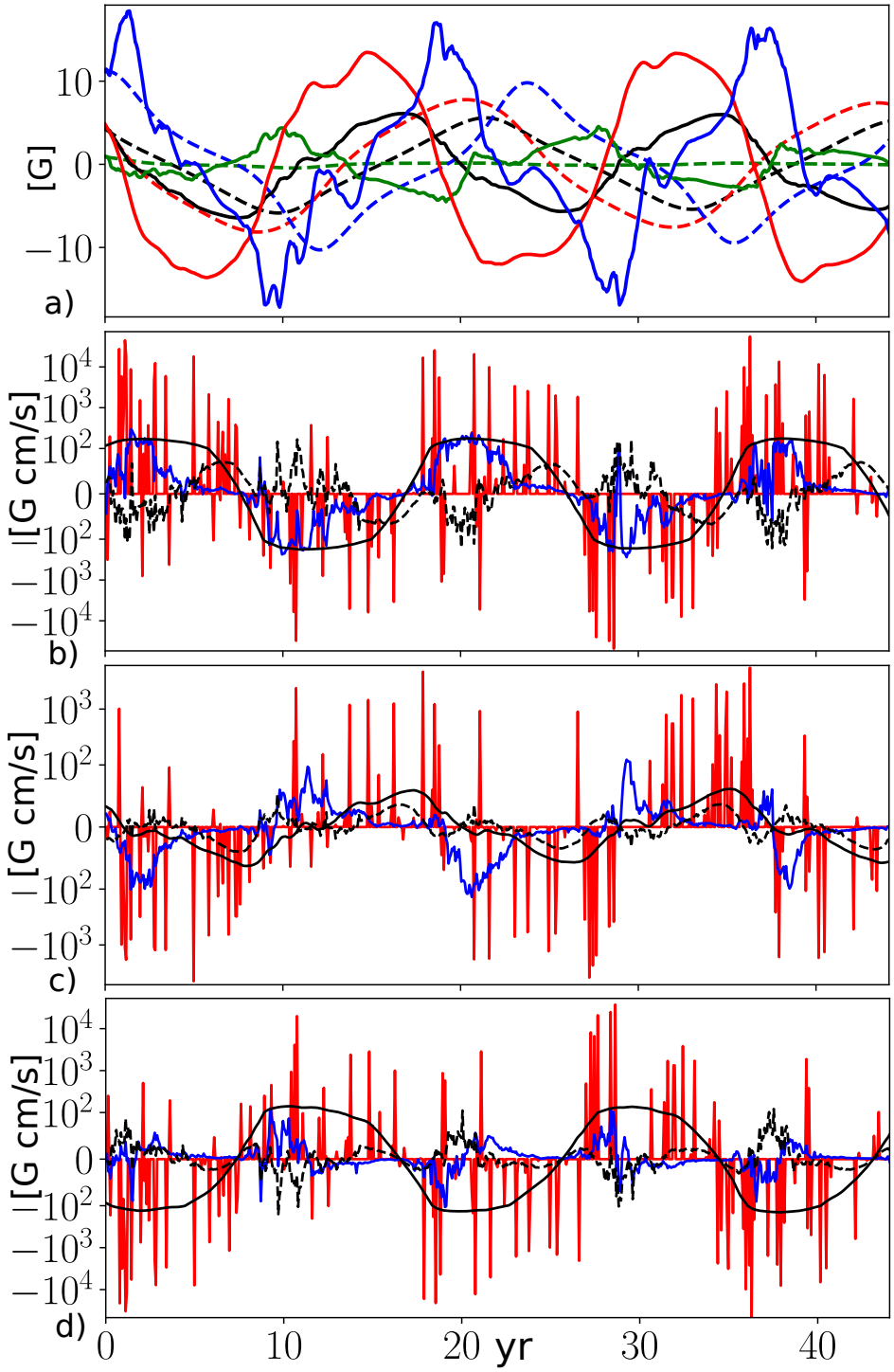

Figure 5. a)Evolution of the first three *odd* harmonics, ℓ_1 (black solid line), ℓ_3 (red solid line), ℓ_5 (blue line line) and harmonic ℓ_2 (green solid line) of the axisymmetric radial magnetic field at the surface; the dashed lines show the same for the model without BMRs b) Evolution of the ℓ_0 harmonic of the α effect magnetic field generation at the near surface level r=0.987R, $E_1^{(0)}$ - black solid line, $E_2^{(0)}$ (magnetic helicity effect) - black dashed line, $E_3^{(0)}$ - blue line, and $E_4^{(0)}$ - red line; c) and d) show the same as b) for the ℓ_2 and ℓ_4 harmonic of the α effect magnetic field generation.

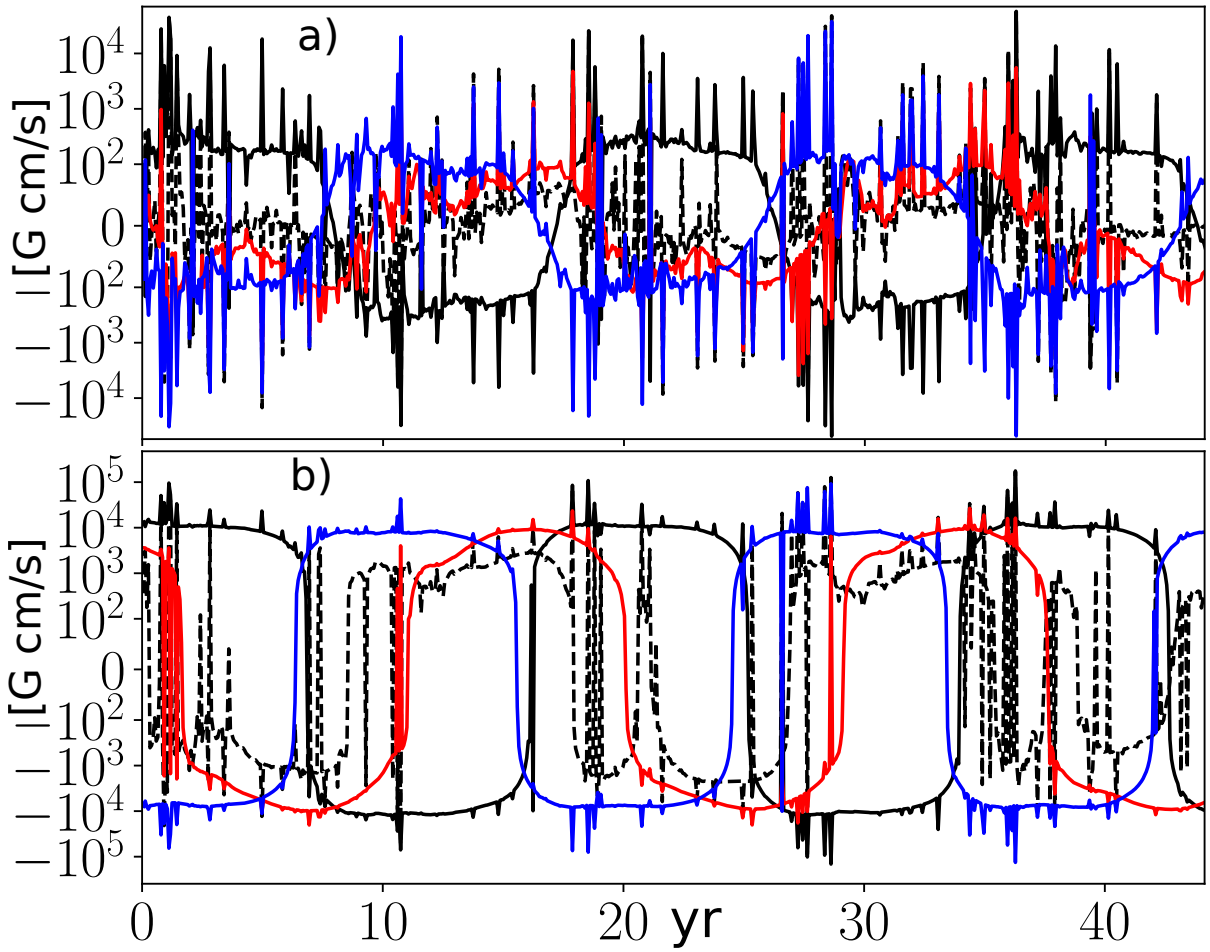

Figure 6. a)Evolution of the first three *even* harmonics, ℓ_0 (black solid line), ℓ_2 (red line), ℓ_4 (blue line) and the odd harmonic ℓ_1 (black dashed line) of the $\mathcal{E}^{\alpha}_{\phi}$ (see the Eq(25)) at the near surface level r=0.987R; b) the same as a) for r=0.86R.

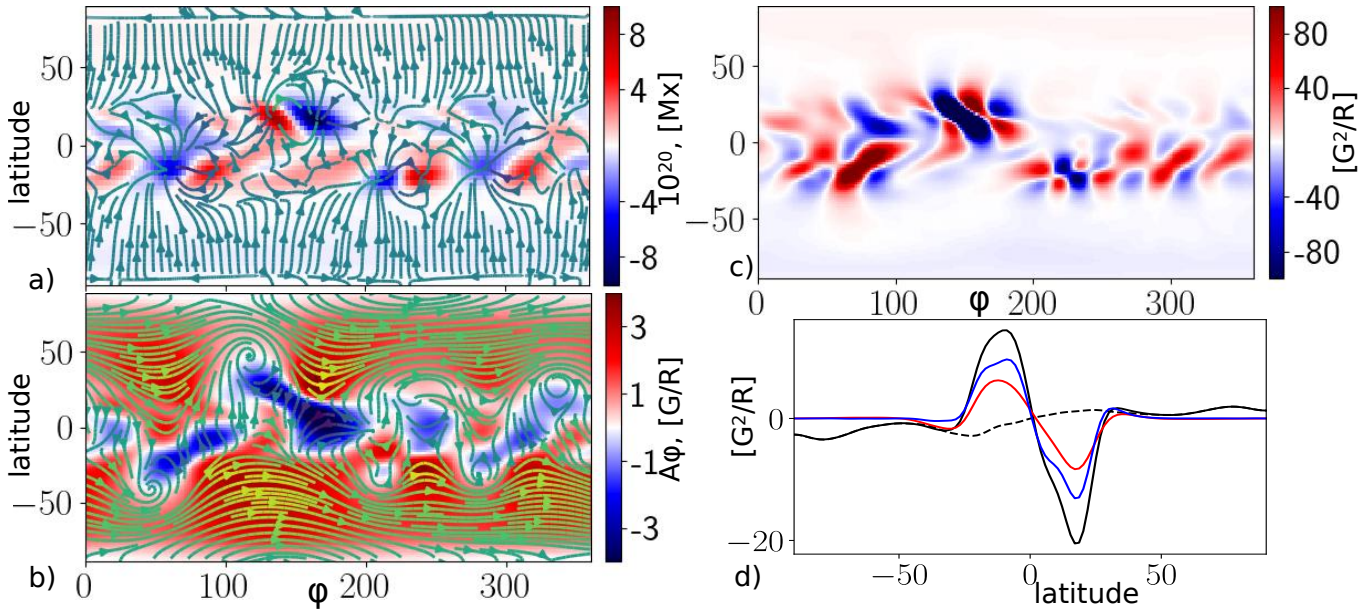

Figure 7. a)Snapshot of the density flux of the radial magnetic field (color image) and sreamlines of the surface magnetic field (color measure the strength of B_ϕ component); b) the vector potential A_φ (color image) and sreamlines of the surface vector-potential;c) the snapshot of the magnetic helicity density; d) the longitudinally averaged magnetic helicity density: black solid line shows the total magnetic helicity density $\langle \mathbf{A} \rangle \cdot \langle \mathbf{B} \rangle$, the dashed line shows $\overline{\mathbf{A}} \cdot \overline{\mathbf{B}}$, the red line - $\tilde{A}_\varphi \tilde{B}_\varphi$, and the blue line - $\tilde{A}_\theta \tilde{B}_\theta$.

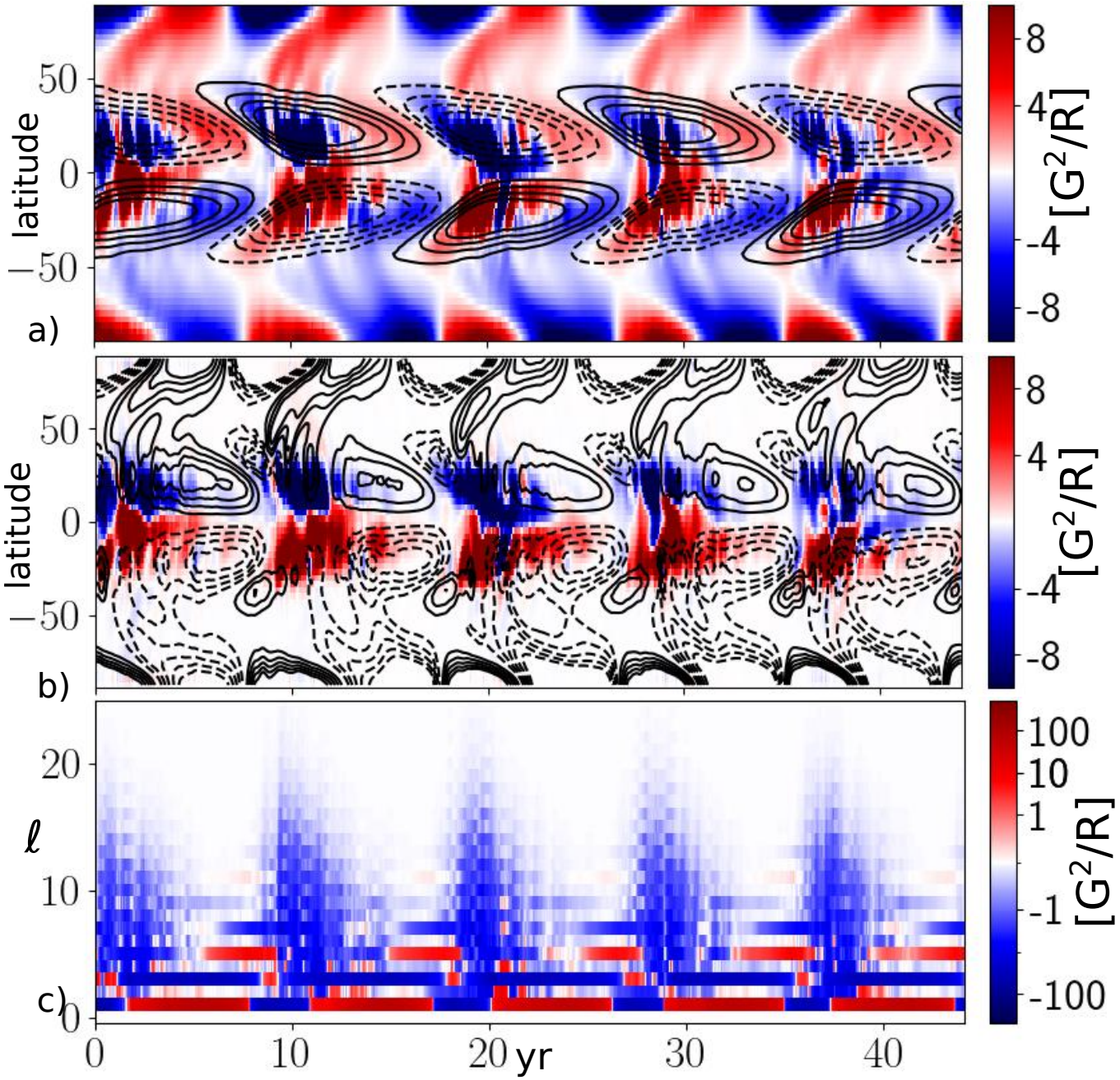

Figure 8. a) The time-latitude diagram of the total magnetic helicity of the large-scale field (color image), contours ±1kG show the toroidal magnetic field in the subsurface layer r=0.9R; b) the color image shows the magnetic helicity density of the non-axisymmetric magnetic field, and contours show the same (in the same range) for the axisymmetric magnetic field; c) the helicity proxy spectrum, H_ℓ^+ evolution (see, the Eq.27) at the surface.